HYDROLOGICAL PROCESSES
Hydrol. Process. **25**, 2456–2470 (2011)
Published online 17 February 2011 in Wiley Online Library
(wileyonlinelibrary.com) DOI: 10.1002/hyp.8022

Modelling hydrological processes influenced by soil, rock and vegetation in a small karst basin of southwest China

Zhicai Zhang,[1] Xi Chen,[1]* Anas Ghadouani[2] and Peng Shi[1]

[1] *State Key Laboratory of Hydrology-Water Resources and Hydraulic Engineering Hohai University, Nanjing 210098, China*
[2] *School of Environmental Systems Engineering, The University of Western Australia, Western Australia, Australia*

Abstract:

Hydrological processes in karst basins are controlled by permeable multimedia, consisting of soil pores, epikarst fractures, and underground conduits. Distributed modelling of hydrological dynamics in such heterogeneous hydrogeological conditions is a challenging task. Basing on the multilayer structure of the distributed hydrology-soil-vegetation model (DHSVM), a distributed hydrological model for a karst basin was developed by integrating mathematical routings of porous Darcy flow, fissure flow and underground channel flow. Specifically, infiltration and saturated flow movement within epikarst fractures are expressed by the 'cubic law' equation which is associated with fractural width, direction, and spacing. A small karst basin located in Guizhou province of southwest China was selected for this hydrological simulation. The model parameters were determined on the basis of field measurement and calibrated against the observed soil moisture contents, vegetation interception, surface runoff, and underground flow discharges from the basin outlet. The results show that due to high permeability of the epikarst zone, a significant amount of surface runoff is only generated after heavy rainfall events during the wet season. Rock exposure and the epikarst zone significantly increase flood discharge and decrease evapotranspiration (ET) loss; the peak flood discharge is directly proportional to the size of the aperture. Distribution of soil moisture content (SMC) primarily depends on topographic variations just after a heavy rainfall, while SMC and actual ET are dominated by land cover after a period of consecutive non-rainfall days. The new model was able to capture the sharp increase and decrease of the underground streamflow hydrograph, and as such can be used to investigate hydrological effects in such rock features and land covers. Copyright © 2011 John Wiley & Sons, Ltd.

KEY WORDS karst; epikarst fracture; vegetation; distributed hydrological model

Received 1 June 2010; Accepted 20 January 2011

INTRODUCTION

Karst terrain covers about 15% of the world's land area or about 22·2 million km^2, and is home for around 1 billion people (17% of the world's population) (Yuan and Chai, 1988). About 25% of the world's population is supplied largely or entirely by karst waters, including deep carbonate aquifers (Ford and Williams, 1989). One of the largest, continuous karst areas in the world is located in Yunnan-Guizhou Plateau of southwest China. Carbonate rocks occupy 41·31% of the total area of $730{\cdot}6 \times 10^3$ km^2. The distribution of thick carbonate rocks and thin carbonate rock interbeds is $540{\cdot}8 \times 10^3$ km^2 and $189{\cdot}8 \times 10^3$ km^2, about 30·90 and 10·73% of the total area, respectively (Lu, 2007). The hilly mountainous areas with typical cone karst and cockpit karst comprise about 73% of the southwest karst area of Guizhou province, China. About 41·2% of the land experiences soil erosion and loss of water due to deforestation and agriculture. Soils in the karst region, developed on carbonate rocks, are generally thin (30–50 cm in thickness), and the epikarst zone (the near-surface weathered zone of the exposed carbonates) in the karst basin has a key role for water storage and movement, as well as for transpiration of vegetation root systems.

The simulations of the karstic hydrological processes are mostly focused on groundwater flow and spring hydrographs. These were achieved by using two main modelling methods: (i) physically distributed models, and (ii) lumped models, with two different approaches either as black- or grey-box or reservoirs (Fleury *et al*., 2007). The lumped models were developed and used for simulating karst aquifer function, and especially spring hydrographs. A black-box model represents a completely unknown system, and a grey-box model corresponds to a system where part of the behaviour is understood and part is obscure (Hao *et al*., 2006). The reservoir models are developed using a simple discharge equation between linked reservoirs, and have the advantages of keeping a memory of the previous water height in each reservoir and simulating the main steps of the aquifer functioning (Fleury *et al*., 2007). The lumped models are an option for karstic hydrological modelling primarily because very few observations are needed; the main disadvantage is a lack of information on spatial variability in flow directions.

* Correspondence to: Xi Chen, State Key Laboratory of Hydrology-Water Resources and Hydraulic Engineering, Hohai University, Nanjing 210098, China. E-mail: xichen@hhu.edu.cn

Distributed modelling of groundwater dynamics in the saturated zone is usually based on numerical groundwater models, e.g. MODFLOW (Harbaugh, 2005) and FEFLOW (Diersch and Michels, 1995), in the same way as for porous or fractured aquifers (Scanlon *et al*., 2003). They are improved to be able to represent the flow conditions in the saturated zone of karst aquifers in an underground conduit-and-fracture network through a porous matrix, like MODFLOW-DCM (Sun *et al*., 2005). However, application of these models in the karst area of southwest China is very difficult because most basins are located in the mountainous areas where observation data of the groundwater table are not available. Moreover, the groundwater-based models do not describe spatial distribution of soil moisture content, hillslope surface water or evapotranspiration (ET) from soil or epikarst. Therefore, these kinds of models are not suitable for estimation of eco-hydrological relationships.

Distributed hydrological models, like TOPMODEL (Beven and Kirkby, 1979) and the distributed hydrology-soil-vegetation model (DHSVM) (Wigmosta *et al*., 1994), describe hydrological processes, especially surface, subsurface and groundwater flows, and ET from soil. They are often used to evaluate impacts of climatic change and land use and land cover on hydrology and water resources as they are easily developed to integrate with climate models and ecological processes. However, these hydrological models seldom reflect the hydrodynamics of water movement in the fractured medium.

A practical method for describing subsurface flow in either soil or fracture media is based on Darcy's equation with different expressions of hydraulic conductivity and transmissivity. Teutsch (1993) used an equivalent porous medium, dual continuum approach to simulate a moderate to highly karstified system. One continuum represents moderately karstified zones in low conductivity and high storativity, while the other continuum represents highly karstified zones in high conductivity and low storativity. Hydraulic conductivity and transmissivity of fractured media can be estimated by the 'cubic law' (Király 1969; Snow 1969) if the fracture properties of aperture and spacing are known.

In this study, we improved the distributed hydrology-soil-vegetation model (DHSVM) for describing hydrological processes in both porous and fissure mediums of the karst basin. In the improved DHSVM, a mixed runoff routing method integrating interactions among Darcy flow, fissure flow and channel storage routing was developed. The improved model was applied in a small watershed of Chenqi within the Puding Karst Eco-hydrological Observation Station, Guizhou province of China (Figure 1). After the model was calibrated and validated based on the observation data of streamflow, vegetation interception and soil moisture contents, it was used to quantify hydrological processes influenced by vegetation, soil, and fracture features of the karst basin.

METHODOLOGY

DHSVM

Distributed Hydrology-Soils-Vegetation Model (DHSVM) is a physically based distributed parameter model that provides a DEM based representation of a watershed (Wigmosta *et al*., 1994). The spatial scale of the representation is based on the grid size of the DEM. The model consists of a two-layer canopy (overstorey vegetation, understorey vegetation), representation of ET, a two-layer energy balance model for ground snow pack, a multilayer unsaturated soil model, a saturated subsurface flow model, and a grid-based overland flow routing. The DEM provides the topographic controls on the incoming short-wave radiation, precipitation, air temperature, and downslope water movement. Grid cells are assigned vegetation and soil characteristics and are hydrologically linked through surface and subsurface flow routing.

Karstic flow system and modelling methods

Karstic flow system. From the hydrological aspect, the vertical profile of a karst zone could be divided into three zones as shown in Figure 2: an uppermost soil and underlying epikarst zone, an infiltration zone and a deep conduit system. Due to effects of CO_2 supply and water flow on soluble carbonate rocks, the network of epikarst fissures through which percolation water passes is widened by dissolution near the surface. Therefore, near the surface, epikarst has a large permeability, offering a fast water infiltration. As the extent and frequency of widening diminishes gradually with depth, epikarst permeability diminishes with depth (Ford and Williams, 2007). Consequently, after recharge, percolating rainwater is retained near the base of the epikarst leading to the formation of an epikarstic aquifer (Williams, 2008).

Part of the fully saturated epikarst zone during a heavy rainfall period may form overland flow, and the remainder of the temporarily stored water flows via the vertical shaft system into conduit systems of the deep aquifer. Since the infiltration flow via the vertical shaft system of the infiltration zone into the conduit system of the aquifer, as shown in Figure 2, is fast (Fleury *et al*., 2007), regulation of the infiltration zone for delaying and storing the karst recharge can be neglected.

Groundwater in deep aquifers flows through interconnected conduits and cave systems, and eventually flows out of the basin as a spring (Figure 1). Due to rich rock fractures and the underground conduit system, streamflow hydrographs for the karst region of southwest China present a steep rise and decline (Chen *et al*., 2008).

Evapotranspiration through vegetation depends on vegetation species and soil and rock fractures. According to investigation by Xiang *et al*(2004), most vegetation roots concentrate in shallow soil and underlying rock fractures in a depth less than 1 m. Tree roots seldom extend to several meters depth due to the hard rock in the karst region. About 70% of root product is within 30 cm depth of soil below the ground surface. Soil water and epikarst water

are main water sources for plant uptake in the karst forest area. Based on stable isotope analysis of water sources of mountain plants on south China karst plateau by Wang *et al*. (2008), it was estimated that he proportion of water uptake by plants was 35 and 50% in the shrub and the forest, respectively.

Multilayer unsaturated zone model. The soil and epikarst zone has the role of delaying the reservoir karst recharge (Aquilina *et al*., 2006; Bakalowicz, 1995; Einsield, 2005; Perrin *et al*., 2003) and offering water for plant uptake. Based on the original DHSVM structure, a multilayer model is used for accounting soil moisture and epikarstic flow dynamics:

$$d_1(\theta_1^{t+\Delta t} - \theta_1^t) = P_0 - P_1(\theta_1) - E_{to} - E_{tu} - E_s + V_{sat} - V_r \quad (1)$$

$$d_2(\theta_2^{t+\Delta t} - \theta_2^t) = P_1(\theta_1) - P_2(\theta_2) - E_{to} + V_{sat} \quad (2)$$

$$d_3(\theta_3^{t+\Delta t} - \theta_3^t) = P_2(\theta_2) - P_3(\theta_3) + (Q_{\sin}^t - Q_s^t)\Delta t \quad (3)$$

where d_1, d_2 are soil or/and epikarst thickness of the upper and lower rooting zones, respectively, d_3 is the left epikarst thickness perched by saturated water, θ_n ($n = 1, 2, 3$) is the average soil moisture content of nth zones, P_0 is the volume of infiltrated rainfall, V_{sat} is the volume of water supplied by a rising water table, V_r is the volume of return flow (generated when a rising water table reaches the ground surface), E_{to} and E_{tu} are ET from overstorey vegetation (o) and understorey vegetation (u), respectively. E_{to} for vegetation root uptake from the upper and lower layers is usually dependent on density

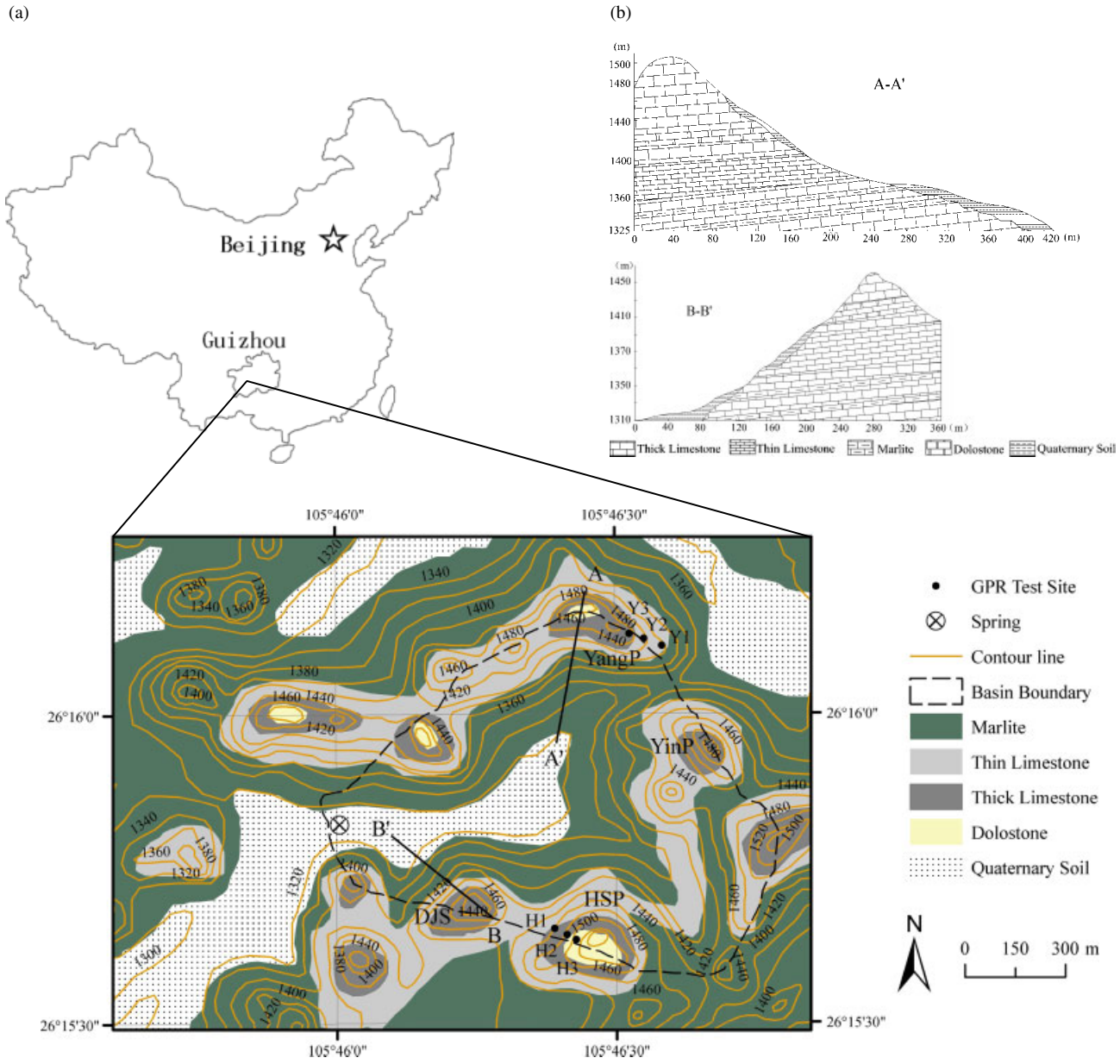

Figure 1. Topography and geology in Chenqi basin (a), Geological profile A–A′ and B–B′ (b), Ground Penetrating Radar profile (c), note: the left side of y axis is the time between antenna radiating radio waves to receiving the reflected return signals, and the right side is the calculated depth with the transmitting time and velocity of radio waves in medium

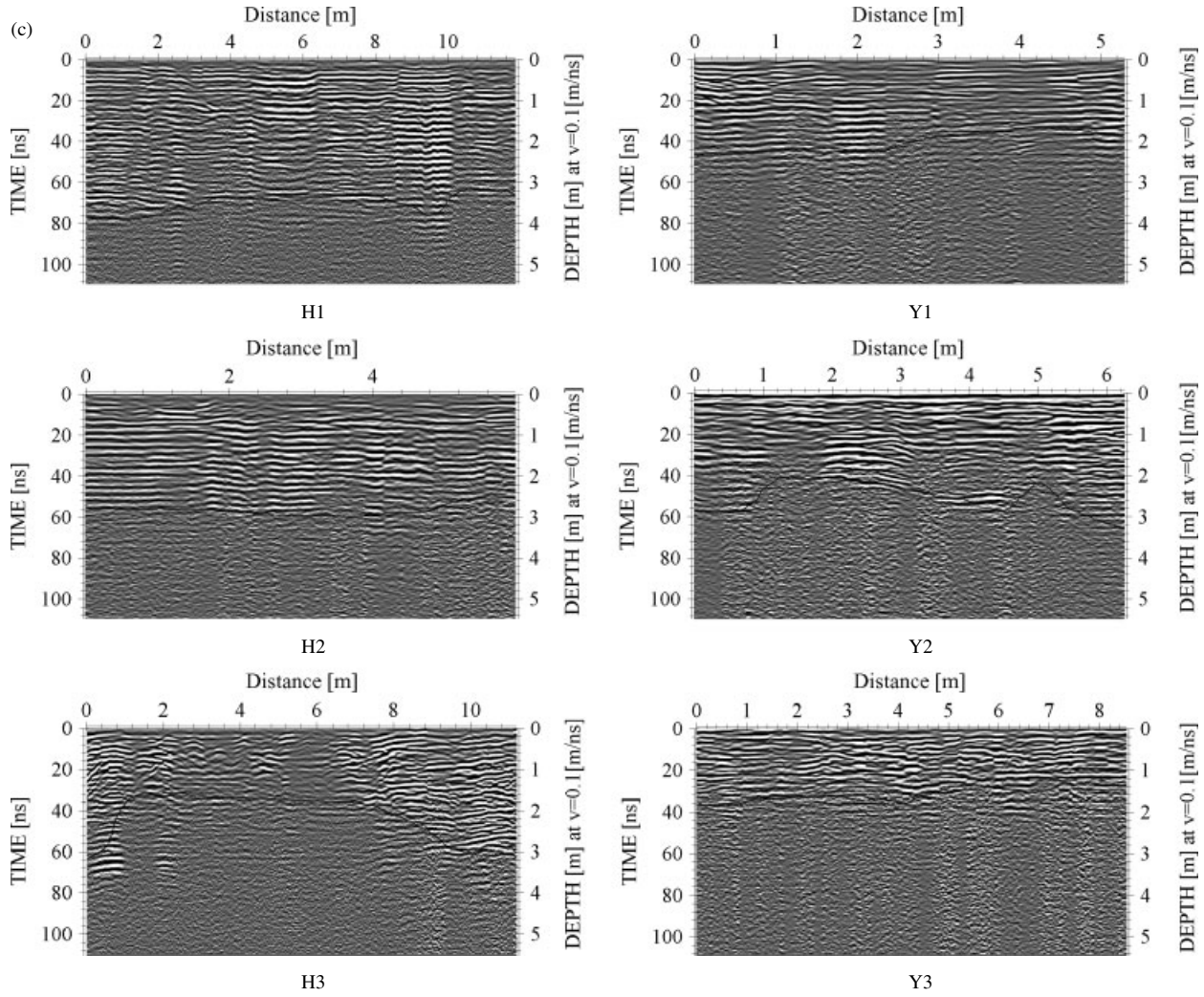

Figure 1. (*Continued*)

of root extension. E_s is soil evaporation, $P_n(\theta)$ ($n = 1, 2, 3$) is downward volume of water discharged from nth zones over the time step, and $Q^t_{\sin}$ and Q^t_s are subsurface flow rate to passing in and out the epikarst zone, respectively.

Vertical infiltration and percolation in soil and fracture. An equivalent hydraulic conductivity $K_v(\theta)$ as follows could be used to compute infiltration and percolation $P_n(\theta)$ based on Darcy's law assuming a unit hydraulic gradient:

$$P_n(\theta) = K_v(\theta) \tag{4}$$

For the uppermost soil, the Brooks-Corey (Brooks and Corey, 1964) equation is used to calculate hydraulic conductivity:

$$K_v(\theta) = K_v(\theta_s)\left[\frac{\theta - \theta_r}{\phi - \theta_r}\right]^{(2/m)+3} \tag{5}$$

where m is the pore size distribution index, ϕ is the soil porosity, and θ_r is the residual soil moisture content. For simplicity, the saturated moisture content θ_s is taken equal to ϕ.

The epikarstic zone consists primarily of fractured media. Hydraulic conductivity and transmissivity in the epikarst zone depend on fracture aperture and spacing. The mathematical formulation of the average velocity of groundwater flow in fractures is given by the 'cubic law' (Király 1969; Snow 1969). The transmissivity and hydraulic conductivity of fractural medium with smooth fractural surface can be expressed as follows (Snow, 1969):

$$T_{i,j} = \frac{\rho g b^3_{i,j}}{12\mu} \tag{6}$$

$$K_{i,j} = \frac{\rho g b^2_{i,j}}{12\mu} \tag{7}$$

where $b_{i,j}$ is the fracture aperture at grid i,j, μ is dynamic viscosity of water, ρ is fluid density, g is acceleration due to gravity.

The equivalent hydraulic conductivity of a rock mass with one parallel set of fractures with rough surface is expressed by:

$$K_{i,j} = C\frac{\rho g b^3_{i,j}}{12\mu s} \tag{8}$$

where s is fracture spacing (m), C is a coefficient which is related with the roughness of the fracture surfaces and

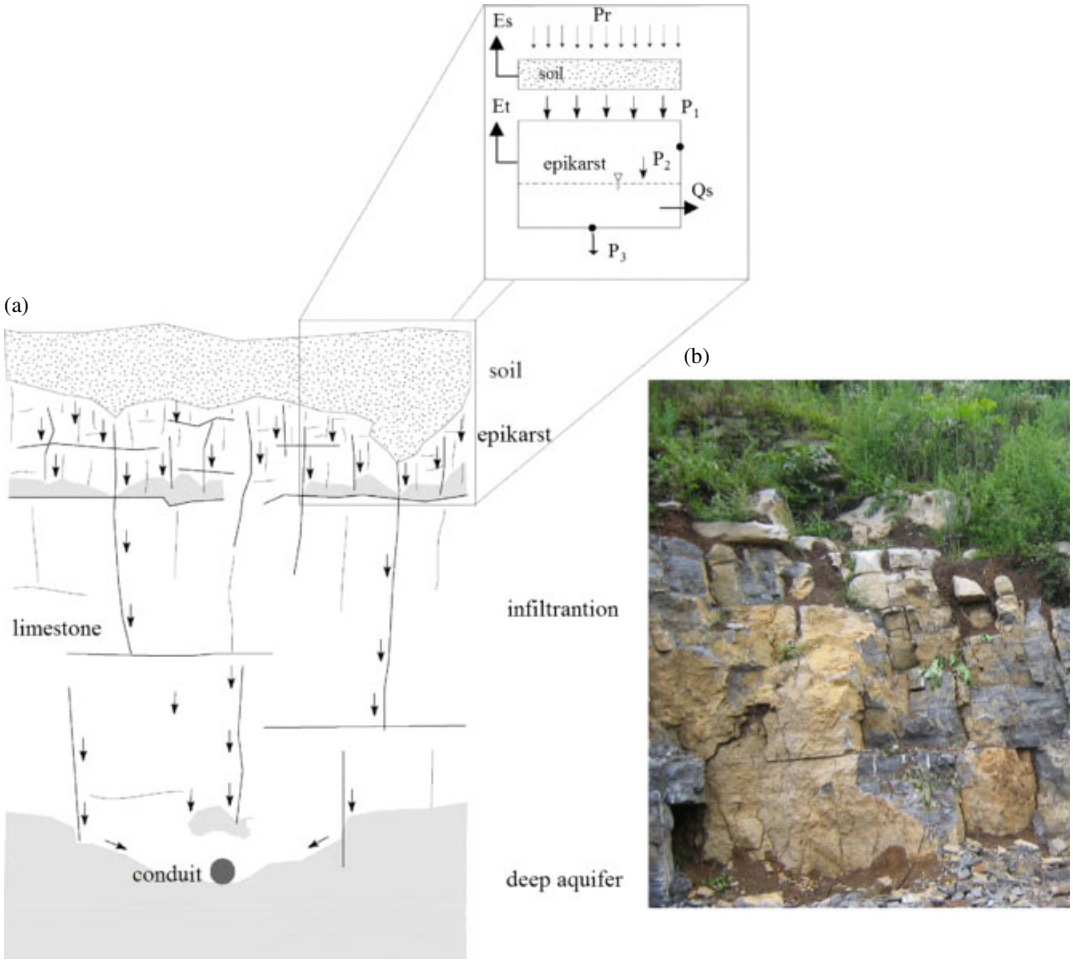

Figure 2. Schematic representation of the vertical flow processes for karst system (modified from Perrin *et al*. 2003) (a), Photo of a profile in the study area (b)

fracture aperture. In an idealized fracture, with a 1 mm aperture and the same spacing, the hydraulic conductivity will be 10^{-3} m/s, similar to that of loose clean sand (Singhal and Gupta, 1999).

Infiltration and percolation $P_n(\theta)$ is estimated by Equation (4) using hydraulic conductivity $K_v(\theta)$, estimated by Equation (5) for the uppermost soil zone and Equation (8) for the epikarst fracture zone. For the uppermost soil zone with partial rock exposure, an equivalent infiltration rate can be estimated by following equation:

$$P_{n,eq}(\theta_n) = K_v(\theta)(1 - f_r) + K_{i,j} f_r \tag{9}$$

where f_r is the ratio of rock exposure.

In the saturated epikarst zone, subsurface water flowing cell by cell is calculated by the following equation with different values of horizontal transmissivities.

$$q(t)_{i,j,k} = w_{i,j,k} f_{i,j,k} T(t)_{i,j} \tag{10}$$

where $w_{i,j,k}$ is the grid (i, j) width at k flow direction, $T(t)_{i,j}$ is hydraulic transmissivity for grid (i, j), $f_{i,j,k}$ is flow fraction for cell i,j in direction k and is usually estimated as topographic slope or groundwater slope $\beta_{i,j,k}$.

Limestone fracture aperture may be as large as 1×10^{-2} m on the exposed surface, decreasing to $1 \times 10^{-3} - 1 \times 10^{-4}$ m in compact and impermeable bed rock (Singhal and Gupta, 1999). As the extent and frequency of fracture widening diminishes gradually with depth (Ford and Williams, 2007), the fracture aperture and spacing can be regarded as exponential decreasing towards the base of the epikarst, resulting in exponential decrease with depth of hydraulic conductivity ($Ks = Ks_{i,j}\ \mathrm{e}^{-\alpha z}$). Thus:

$$T(t)_{i,j} = \frac{Ks_{i,j}}{\alpha_{i,j}}(e^{-\alpha_{i,j} z_{i,j}} - e^{-\alpha_{i,j} D_{i,j}}) \tag{11}$$

where $Ks_{i,j}$ is the lateral component of saturated hydraulic conductivity for cell i, j at epikarst surface and is estimated by Equation (8) with horizontal fractural aperture and spacing, $z_{i,\ j}$ is the distance from the epikarst surface to the water table (positive downward), $\alpha_{i,j}$ is a parameter related to the decay of saturated conductivity with depth, and $D_{i,j}$ is the total epikarst depth.

For a soil matrix, lateral flow direction in the subsurface depends on hydraulic gradient, which is usually assumed as topographic slope and isotropic hydraulic transmissivity $T_{i,j}$ at cell i, j. In karst basins, however, subsurface water in karstic aquifers moves

through an interconnected system of fractures, and strong anisotropy of karst fracture dominates subsurface flow directions as well (Scanlon *et al.*, 2003; Xue *et al.*, 2009). Equation (10) for subsurface water flow at cell i, j in flow direction k should be revised as:

$$q(t)_{i,j,k} = w_{i,j,k} f_{i,j,k} T(t)_{i,j,k} \tag{12}$$

where $T(t)_{i,j,k}$ is hydraulic transmissivity for cell (i, j) at k flsow direction and can be expressed as $p_{i,j,k} \sum_{k=1}^{8} T_{i,j,k}$ in which $p_{i,j,k}$ is equal to $\frac{T_{i,j,k}}{\sum_{k=1}^{8} T_{i,j,k}}$, representing karst fractural anisotropy for cell i, j in direction k. Hence, we developed the following formula to calculate flow fraction $f_{i,j,k}$ for cell i, j in direction k, considering topographic slope or groundwater slope $\beta_{i,j,k}$ and aquifer anisotropy $p_{i,j,k}$:

$$f_{i,j,k} = p_{i,j,k} \beta_{i,j,k} \tag{13}$$

Since the exact location, geometry and hydraulic properties of each fracture are usually unknown, a stochastic model was applied to describe statistical attributes of rock fractures. In absence of field description of fractural anisotropy, the weight $p_{i,j,k}$ can be randomly generated on the basis of uniform distribution of p-values between 0 and 1 in the eight directions (Xue *et al.*, 2009).

Flow routing of underground conduit systems. The conduit systems within aquifers dominated by recharge through internal runoff often exhibit branch patterns as small tributaries which, draining individual closed depressions, merge to form larger drainage channels which ultimately lead to a spring (White, 1999). Simulation of a karst system composed of dendritic paths (e.g. Milanovic, 1981; White, 1988; White and Deike, 1989) may require a great deal of site-specific information for the karst channels and flow conditions (e.g. elevation, slope, fill material, roughness, cross-sectional area, Reynolds number, Froude number, diameter, etc.) (Field and Nash, 1997; Field, 1997).

In this study, flow in the conduit systems is routed using a series of cascading linear channel reaches (Figure 3), with individual hydraulic parameters describe each reach. As the reach passes through grid cells, lateral inflow into the channel reach consists of matrix and fracture flow. Flow is routed between channel reaches as a linear routing algorithm where each reach is treated as a reservoir of constant width with outflow linearly related to storage.

$$Q_{out} = Q_{in} - (V_C^{t+1} - V_C^t)/\Delta t \tag{14}$$

$$V_C^{t+1} = \frac{Q_{in}}{k} + \left(V_C^t - \frac{Q_{in}}{k}\right) \exp(-k\Delta t) \tag{15}$$

$$k = \frac{R_r^{2/3}\sqrt{S_o}}{n\Delta L} \tag{16}$$

where k is coefficient of underground channel storage, R_r hydraulic radius, S_o is hydraulic gradient, ΔL is channel segment, n is Manning's roughness coefficient, Δt is time step, V_c is channel reach storage, Q_{out} is the average outflow from the reach, and Q_{in} is the average rate of lateral and upstream inflow to the reach during the time step.

SITE DESCRIPTION AND OBSERVATION

Site description and field investigation

The small catchment of Chenqi is located in the Puding basin of Guizhou, and has an area of 1·5 km^2 (Figure 1). The study site has a subtropical wet monsoon climate with a mean annual temperature of 20·1 °C. The highest average monthly temperature is in July, and the lowest is in January. Annual precipitation is 1140 mm, with a distinct wet summer season from May to September and a dry winter season from October to April the following year. Average monthly humidity ranges from 74 to 78%. The elevation of the study area varies between 1320 and 1520 m above the sea level (Figure 1(a)). With typical cone karst and cockpit karst geomorphology, the cone peaks of Chenqi catchment are generally 200 m above the adjacent doline depressions, and its catchment surface relief and slope are very steep. Geological properties include dolostone, thick and thin limestone, marlite, and Quaternary soil. Limestone formations with a thickness of 150–200 m lay above

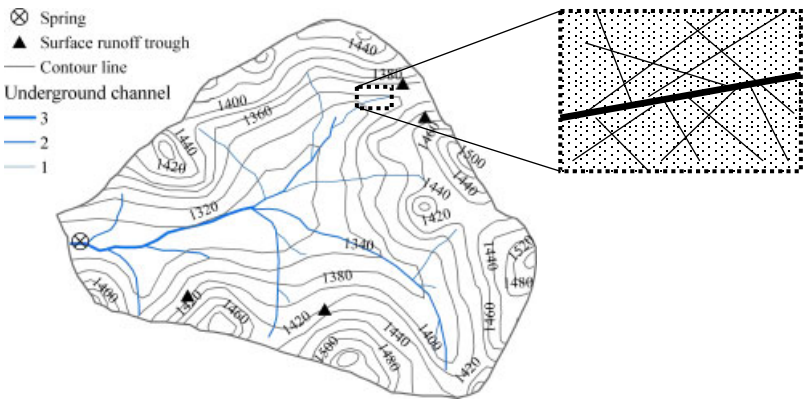

Figure 3. Groundwater channel network

Table I. Characteristics of vegetation, soil and rock fracture on four hillslopes in the study catchment

Hillslope	Land cover	Plant height (m)	Canopy fraction (%)	Soil K_v (10^{-5} m/s)		Rock outcrop rate (%)	Epikarst		
				Upper (0–15 cm)	Lower (15–30 cm)		Thickness (m)	Porosity (%)	K (10^{-3}m/s)
YangP	Shrub	1–2	45	—	—	50	1·5–2·5	—	—
YinP	Forest	2–5	90	4.50	1.00	20	—	—	—
HSP	Shrub (burned area)	1–2 (0)	50 (0)	5.67	0.02	35	2·0–3·5	—	—
DJS	Forest	2–5	85	4.83	1.33	30	—	5·3 (2·4–5·9)	2·56–6·11

Note: Canopy fraction and rock outcrop rate were investigated through typical areas by Peng *et al*. (2008); soil hydraulic conductivity (K_v) was measured using Guelph-Infiltration; epikarst thickness was estimated by Ground Penetrating Radar; its porosity was measured in a profile of DJS, and fracture hydraulic conductivity (K) was measured according to steady rate of infiltration by a ponded water infiltration method in the profile of DJS.

impervious marlite formation (Figure 1(b)). Field investigations using Ground Penetrating Radar (MALA Professional Explorer (ProEx) System) show a rich fractured zone for the epikarst on the two hillslopes of Yangpo (YangP) (Y1–Y3 in Figure 1(c)) and Houshaopo (HSP) (H1–H3 in Figure 1(c)). The thickness usually decreases upward along hillslope. As shown in Figure 1(c) and Table I, epikarst thickness is estimated as 3·5, 2·8, and 2·0 m for the profile of H1, H2, and H3, and 2·0, 2·5, and 1·5 m for Y1, Y2, and Y3, respectively.

The vegetation species include grasses, karst montane deciduous broad-leaved shrubs and evergreens and deciduous broad-leaved mixed forest (Figure 4(a)). According to field investigation by Peng *et al*. (2008) (Table I), the forest areas of Yinpo (YinP) and Dongjiashan (DJS) have higher tree, denser canopy cover, and less rock outcrop rate, compared with those in the shrub area of YangP and HSP. In the grass area, the canopy fraction is about 80% and rock outcrop rate is 35%. Rate of rainfall interception by forest is 13·2% on average, ranging between 3 and 25% for rainfall events with the total of 6·4–90·4 mm. For shrub areas, the rate of interception is about 9·7% on average. Proportions of ET E_{T0} for the upper and lower rooting zones in Equations (1)–(3) are assumed as 0·5 and 0·5 for forest, 0·65 and 0·35 for the shrub, and 0·8 and 0·2 for the grass; this is according to investigation of vegetation root distribution by Xiang *et al*(2004) and isotope analysis of water sources for mountain plant uptake on the southern China karst plateau by Wang *et al*. (2008).

Distribution of soil properties, e.g. soil types, composition and density, were determined through field investigation and laboratory experiments from 49 soil samples. Generally, soil of the upper 20 cm is classified as two types of loam in the low and depression areas, and sand loam in the middle and upper hill areas (Figure 4(b)), with bulk density of 0·66–0·90 g/cm^3 and porosity of 0·2–0·4, respectively. The lower layer is primarily brown clay with high calcium content (Figure 4(b)); its density is 1–1·28 g/cm^3 and porosity 0·42–0·48.

In situ experiments for the determination of saturated hydraulic conductivity (K_v) of soil were conducted at 15 measuring points using Guelph-Infiltration (GUELPH) (Table I). The upper soil K_v varies from $4{\cdot}5 \times 10^{-5}$m/s for loam to $5{\cdot}67 \times 10^{-5}$m/s for sand loam. Shallow soil, with depth less than 15 cm overlying fractured bedrock, significantly increases K_v, which can be as large as $1{\cdot}47 \times 10^{-4}$ m/s. Soil below 0·5 cm depth is usually compacted and K_v is less than $1{\cdot}0 \times 10^{-5}$ m/s (Chen *et al*., 2009).

Basing on field observations of rock fracture distribution at 22 sites, the mean fracture aperture was estimated to be around $13{\cdot}6 \times 10^{-3}$ m with standard deviation of $15{\cdot}7 \times 10^{-3}$ m and the mean fracture spacing was determined to be 0·142 m with a standard deviation of 0·0986 m. Exposed fractural apertures larger than 3×10^{-3} m are mostly filled with soil; for apertures less than 3×10^{-3} m, mean fracture aperture is $1{\cdot}55 \times 10^{-3}$ m with a standard deviation of $0{\cdot}705 \times 10^{-3}$ m. Field investigation on a profile of DJS in Chenqi catchment (Figure 2(b) and Table I) demonstrates that average karst fracture porosity is 5·3%, varying from 6·9% in the upper epikarst layer (less than 2 m) to 2·4% in the lower layer about 2–5 m below ground surface, within a range between 1 and 10% for epikarst fractures (Smart and Friederich, 1986; Gouisset, 1981; Williams, 1985). The measured K for fracture apertures in $1–2 \times 10^{-3}$ m is between 2·56 and $6{\cdot}11 \times 10^{-3}$ m/s according to steady rate of infiltration, using a ponded water infiltration method.

Observation data and watershed digitisation

A set of meteorological and eco-hydrological observation stations were established in June 2007 within the Chenqi catchment. Three meteorological stations (15-Channel HOBO Weather Station) are located at hills of DJS, HSP, and YangP with forest, grass, and shrub covers, respectively. Precipitation, air temperature and pressure, relative humidity, wind speed, and radiation are recorded in a time interval of five minutes. Four groups of soil moisture probes at the depths of 30 cm below

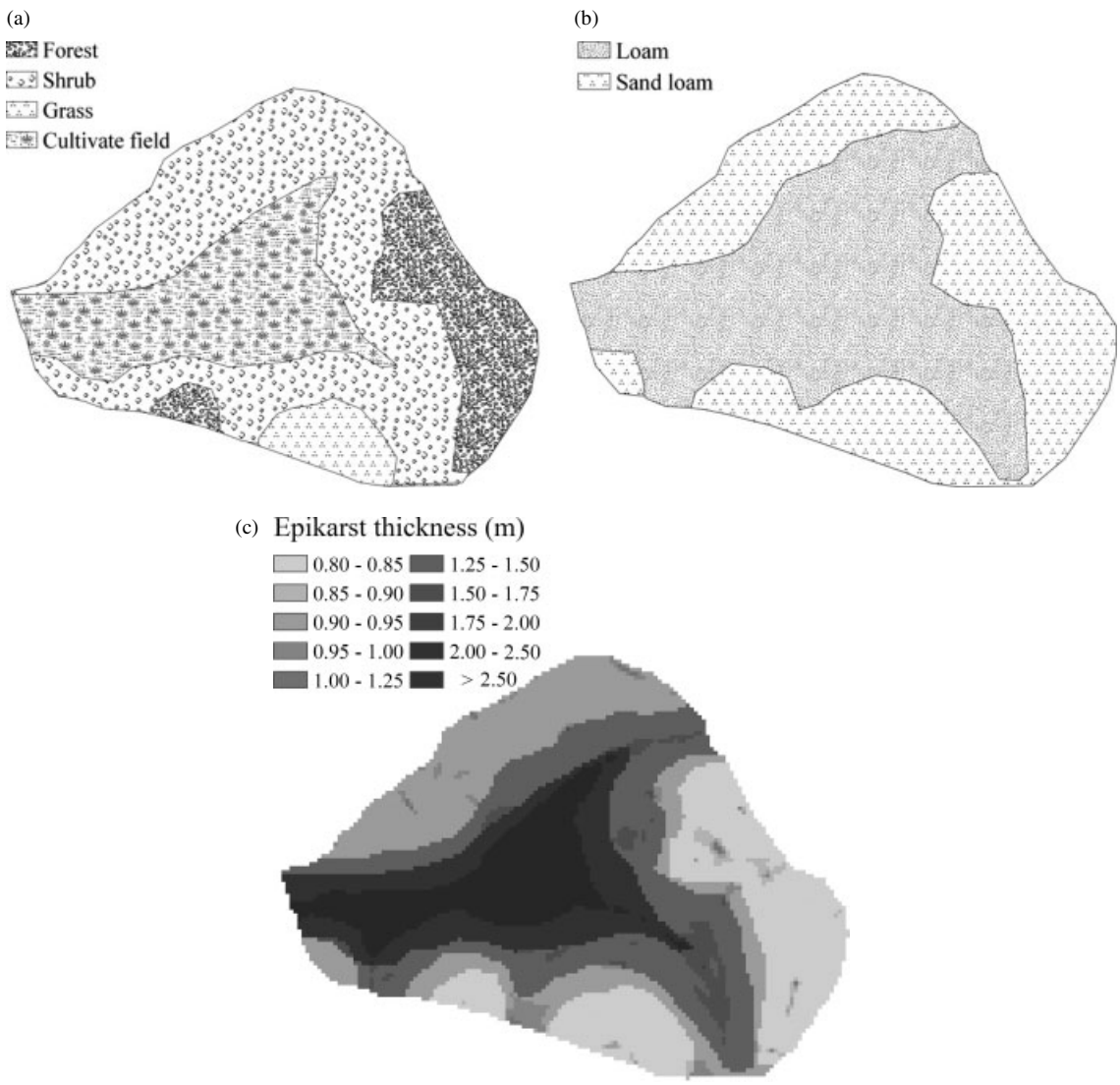

Figure 4. Classification of vegetation (a), soil (b), and distribution of epikarst thickness (c)

the ground surface were installed at DJS, HSP, YinP, and YangP, automatically recording soil moisture content every five minutes. Fifty rainfall collection tubes, with a diameter of 29 cm, were placed under the forest and shrub areas to collect penetrating rainfall. An automatic water level observation station (GREENSPAN) was installed at the catchment outlet to record water level at every 15 min interval.

Meteorological observations demonstrate that forest canopy shades the soil and consequently prevents direct radiation absorption and decreases surface wind speeds, resulting in lower temperature (T) and higher humidity (Figure 5). Daily irradiance at the ground surface within 10–20 cm high grass was 118·2 W/m^2, much greater than 11·1 W/m^2 under 3–12 m high forest. The daily mean relative humidity was 86·3 and 95·5% for the grass and forest cover, respectively. The daily mean air temperature at 1·2 m height is 17·5 and 17·3 °C, and daily mean underground air temperature at 20 cm depth is 19·65 and 17·72 °C for the grass and forest cover, respectively.

The gridded DEM from model computation was derived from the 1 : 10 000 digital topography map from the Puding Karst Ecosystem Observation Station, Guizhou Province, China. The resulting rectangular subset, a 10 m × 10 m resolution DEM containing 16 950 pixels (113 rows by 150 columns), was analysed to delineate the basin boundary. In the DHSVM, a soil class is assigned to each model pixel. Weighted averages of percentage sand, silt, and clay were calculated for each soil class.

The average soil thickness over the calcareous rock is 30 cm. Spatial distribution of the soil thickness is derived from the digital elevation model (DEM). The thickness ranges from 0 for exposed rock areas to 2·0 m for the lower cultivated areas. Spatial distribution of the epikarst thickness, ranging from 0·8 to 4·8 m and the average epikarst thickness being 2·5 m, is generated based on terrain because epikarst thickness is larger in lower flat areas and smaller on steeper hillslopes (Tan, 2005).

Using statistical results of fractural features from field investigation, we mapped fractures onto a

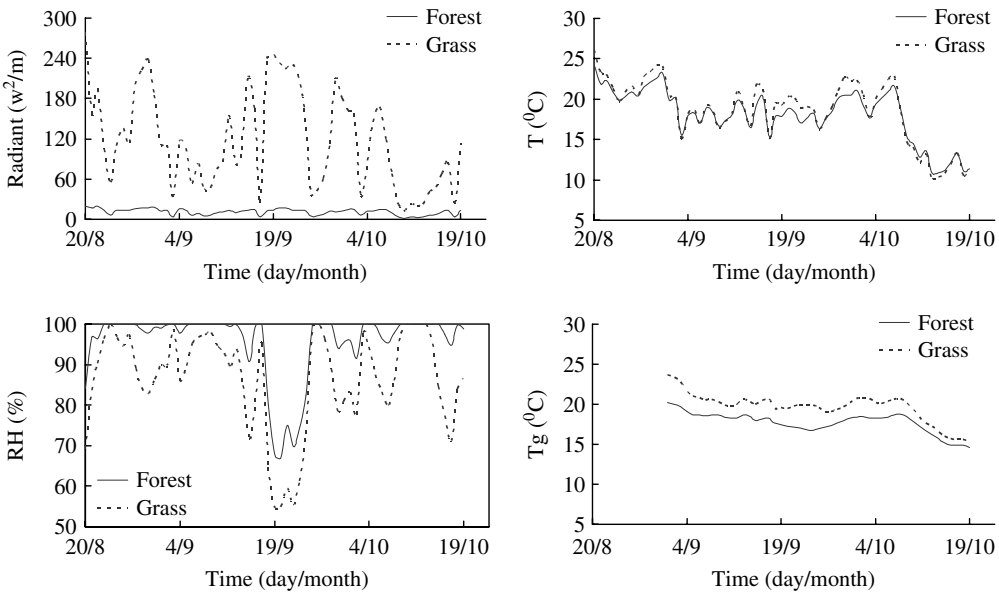

Figure 5. Observed radiant air temperature (T) and relative humidity (RH) at a height of 1·2 m, and underground temperature (Tg) in 0·2 m depth in forest (DJS) and grass (HSP) areas

two-dimensional domain ($x-y$ plane) with the third dimension assumed to be decreasing with depth to groundwater. Distributions of the fracture aperture and spacing on the ground surface in the vertical direction are randomly generated and follow a normal distribution function centred around $1{\cdot}55 \times 10^{-3}$ m, with a variance of $0{\cdot}705 \times 10^{-3}$ m for aperture, and 0·142 m with a variance of 0·0986 m for fracture spacing. The weight p of fracture anisotropy is randomly generated on the basis of uniform distribution of p value between 0 and 1 in the eight directions. Thus, spatial distribution of K_s value can be estimated by Equation (8).

The underground channel drainage network was investigated in detail using tracers and Ground Penetrating Radar. The large underground channels (Figure 3) are located in the lower area of the basin as accumulating floodwater in the lower areas of the valleys dissolves any limestone it touches (Kovács, 2003). GIS analysis was used to determine the channel orders following the Horton ordering scheme, as well as to assign mean values of channel width, depth, and Manning roughness for each order. Three orders of the underground channel network shown as Figure 3 were generated, ranging 1–3 m for channel depths and 0·3–1·5 m for widths.

DETERMINATION OF MODEL PARAMETERS

Procedures for parameter determination

Parameters of hydrological models are usually determined through model calibration according to basin outlet flow discharges. Calibration of physically based distributed models such as the DHSVM requires particular attention to the number of parameters used (e.g. Beven, 1989). Equivalence of different parameter combinations (parameter equifinality) is usually expected, and this causes non-uniqueness of the model calibration. The problem of parameter equifinality can, to some extent, be overcome by adding additional sources of data (e.g. parameterisation results of other basins with similar land surface conditions, field experiment results) and by considering different hydrologic processes that can be separated using the observation data (e.g. soil moisture content and flow discharges).

In this study, the model parameters were determined as follows: (1) Parameters related with vegetation were determined on the basis of Land Data Assimilation System (LDAS) (http://ldas.gsfc.nasa.gov/LDAS8th/MAPPED.VEG/LDASmapveg.shtml) and the field observation of vegetation interception (Figure 6). Except for hydraulic conductivity, parameters related with soil properties, such as porosity, field capacity, and wilting point, were determined by field experiments and laboratory analysis. (2) Field measured soil hydraulic conductivities are used as initial values for model calibration and initial pore size distribution index m references UNSODA (Leij *et al*, 1996). The final values of soil hydraulic conductivities and other soil related parameters (e.g. α and

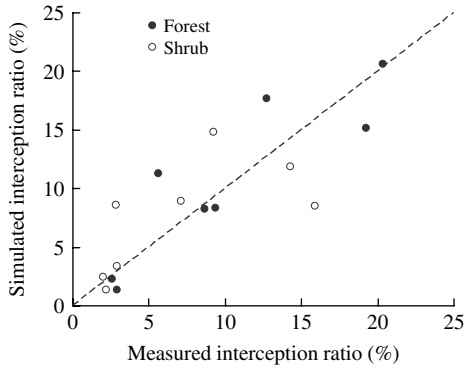

Figure 6. Simulated and measured interception rate of forest and shrub canopy

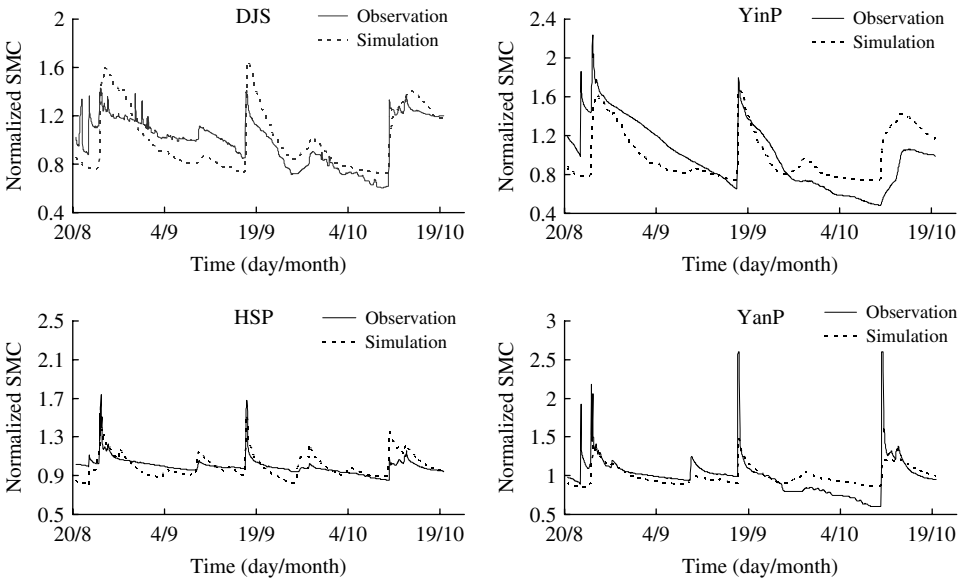

Figure 7. Observed and simulated results of normalized SMC

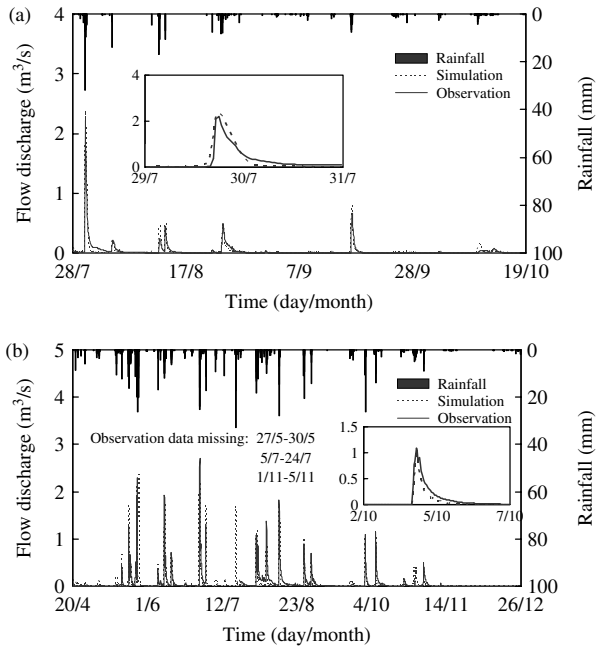

Figure 8. Observed and simulated streamflow for model calibration (a) and validation (b)

m in Equations (5) and (11)) are further calibrated making use of soil moisture content (SMC) data measured at the four sites (Figure 7). (3) Hydraulic conductivities of epikarst and conduit roughness were calibrated using the basin outflow hydrograph (Figure 8); the calibrated hydraulic conductivities represent catchment average values. Their spatial distribution was described according to spatial statistical results of fractural features.

In each calibration step, the four large flood discharges from 28 July 2007 to 19 October 2007 were used for the model initiation and calibration, and the period from 20 April 2008 to 31 December 2008 was held back for the verification. The computation step is 1 h.

Model calibration and validation

Simulation of soil moisture contents. The dynamics of SMC are influenced by soil properties, upper and lower boundary conditions: land surface, including climate and vegetation, and underlying epikarst. Climate and vegetation canopy influences can be calculated using the two-layer canopy ET package of DHSVM. The underlying epikarst boundary can be assumed as having a large infiltration rate without water ponding on the soil–epikarst interface as the epikarst fracture Kv is usually much larger than that of the upper soil, and thus, the underlying permeability does not influence downward water percolation from the upper soil zone ($P_1(\theta)$ in Equation (1)). Therefore, we focused on calibration of the upper soil hydraulic conductivities which strongly influence infiltration and water flow, and thus, soil moisture content. If the horizontal hydraulic conductivity Ks is assumed to be same as the vertical hydraulic conductivity Kv, the hydraulic conductivities at the soil surface, Kv in Equation (5), is calibrated as $1{\cdot}5 \times 10^{-5}$ and $1{\cdot}6 \times 10^{-5}$ m/s for loam and sand loam, respectively. Exponential decrease coefficient α is 3 and the pore size distribution index m for Equation (5) is 0·19 and 0·20 for loam and sand loam, respectively.

Figure 7 shows that simulated and observed SMCs at DJS, YinP, YangP, and HSP have similar change patterns, represented by the normalized SMC. However, the magnitude of simulated SMC is different from of the observed SMC because simulated SMC represents the average value within the 10 m × 10 m grid, while observed SMC represents a point value from the sensor.

Simulation of streamflow discharges. Generally, the influence of small storage of the thin soil on the hydrograph is not significant compared with epikarst and conduit system in the study area. Epikarst hydraulic conductivity and conduit roughness are regarded as two key parameters controlling the hydrograph. They can

be calibrated based on measured underground flow discharge. For underground flow discharge simulation, three objective functions are selected for evaluating the success of the calibration: the relative volume error R_{ve} between the observed and simulated flows; the root mean squared error RMSE, relating how well the calculated and observed hydrographs compare in both volume and shape; and the coefficient of determination D, relating how well the calculated hydrograph compares in shape to that observed and depends only on timing, not on volume.

The model computation results demonstrate: $R_{ve} = -0{\cdot}018$, RMSE $= 0{\cdot}05$ m^3/s, and $D = 0{\cdot}847$ for the calibration period from 28 July 2007 to 19 October 2007; $R_{ve} = 0{\cdot}157$, RMSE $= 0{\cdot}08$ m^3/s, and $D = 0{\cdot}752$ for the validation period from 20 April 2008 to 31 December 2008. These results illustrate that adjustments to the lateral hydraulic conductivity profile are sufficient to match the outflow hydrograph with reasonable accuracy (Figure 8).

The calibrated roughness coefficient of the fractural surfaces C is 0·5 and, thus, the estimated mean value of horizontal hydraulic conductivities at epikarst surface Ks is $2{\cdot}22 \times 10^{-3}$ m/s. Roughness which controls hydrograph oscillation is 0·025.

The simulated hydrographs can be further validated by statistical results of the surface runoff in the hillslopes of DJS, YinP, HSP, and YangP (see location of surface runoff troughs in Figure 3). Simulated and observed results in Figure 9 show that because of large storage room and high hydraulic conductivity of epikarst fractures, the proportion of surface runoff in the total rainfall amount is less than 1% for a small rainfall event and it then increases exponentially for a heavy rainfall event when the whole epikarst is saturated. For the heavy rainfall event with amount of 90·2 mm on 30 July 2007, the simulated surface runoff is 6·0 mm for DJS, 3·2 mm for YinP, 17·3 mm for HSP, and 10·8 mm for YangP. The thriving forest areas of YinP and DJS produce less surface runoff due to vegetation interception of rainfall. This result is consistent with statistical results from the surface runoff trough by Peng *et.al.* (2008) (Figure 9).

SIMULATION OF SPATIAL DISTRIBUTION OF SMC AND ET

Spatial distribution of the simulated soil moisture content (SMC) and actual ET reveals integrated influences of topography, soil and karst fracture, and land cover on hydrology. Figure 10 shows that just after a heavy rainfall of 90·4 mm/d, SMC at 12 pm, 30 July 2007 primarily depends on topography, e.g. water concentration into low areas. Basin average SMCs for different land covers demonstrate that SMC at the upper soil layer is larger in the lower area of agricultural land than in the hillslopes with forest and shrub covers. However, SMCs are dominated by land covers due to ET after a period of six consecutive non-rainfall days (12 pm, 11 August 2007).

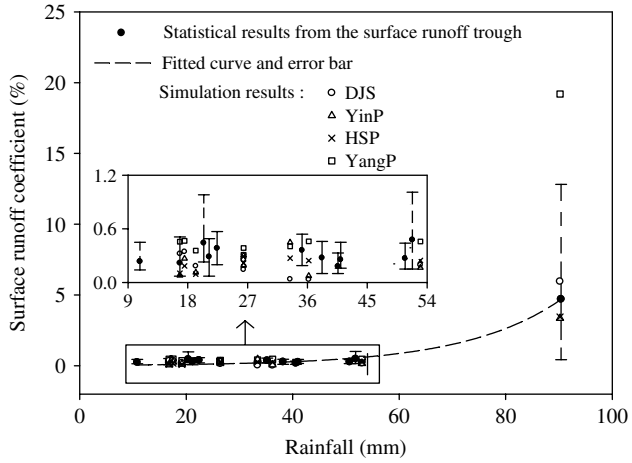

Figure 9. Statistical results of simulated and observed surface runoff. Note: the solid dot represents statistical results of surface runoff collected by troughs

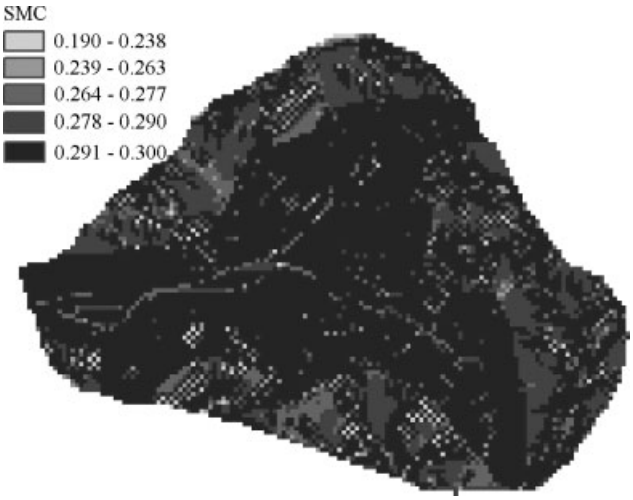

Figure 10. SMC after a heavy rainfall

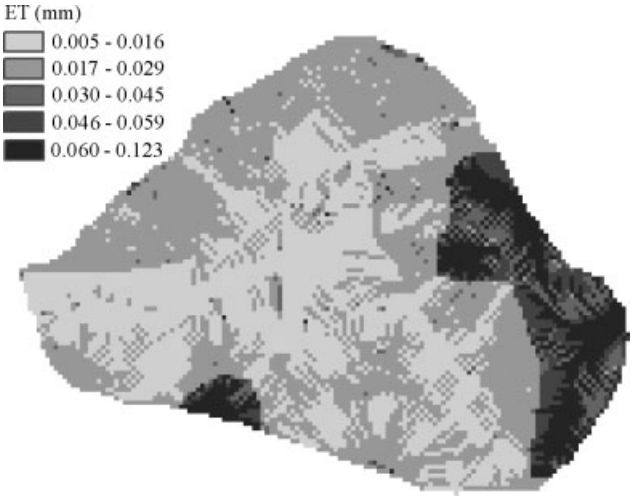

Figure 11. ET after consecutive no-rainfall days

Statistical results from Figure 11 demonstrate that forest ET at 12 pm is 0·053 mm, much larger than 0·016 and 0·012 mm in the shrub and bare soil areas,

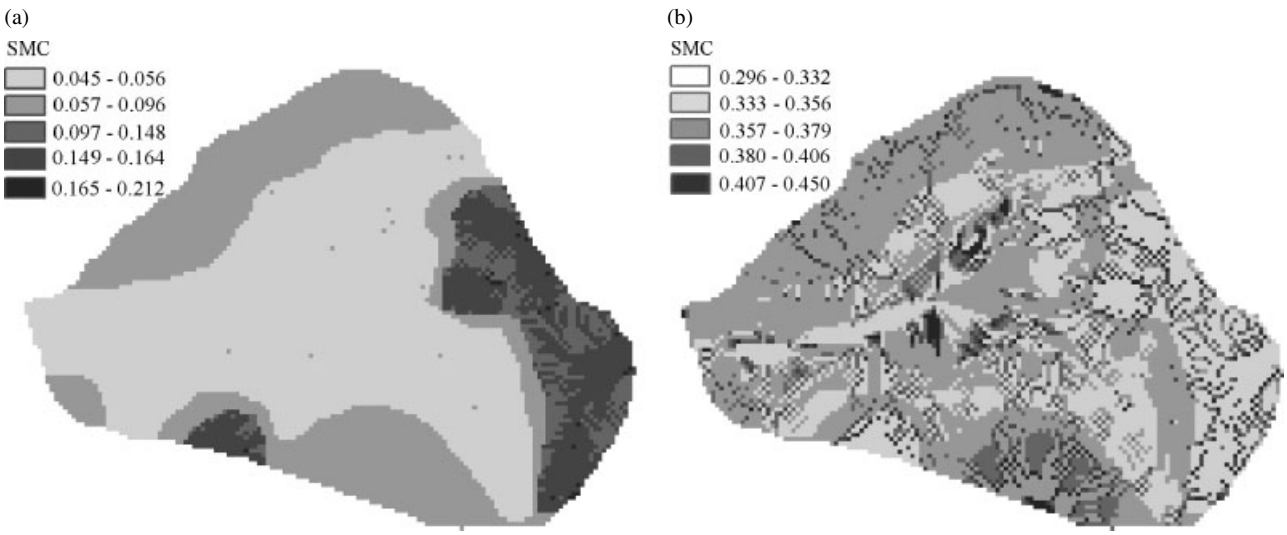

Figure 12. SMC for the upper layer (a) and the lower layer (b) after consecutive no-rainfall days

respectively. Figure 12 shows that SMC loss due to larger ET from the deep layer for forest, compared with those from the shallow layer in the shrub and bare soil areas. The upper layer soil in the forest cover areas has larger SMC than the shrub and agricultural areas (0·15 for forest *vs* 0·065 and 0·05 for shrub and agricultural areas, respectively). Conversely, the lower layer in the forest cover areas has less SMC than the shrubs agricultural areas (0·32 for forest *vs* 0·37 and 0·34 for shrub and agricultural areas, respectively). Spatial variation of the upper SMC is closely related with land covers, but the lower layer SMC is sporadic, indicating that the random distributed epikarst fractures has significant influence on holding of its upper layer SMC.

EFFECT OF EPIKARST FRACTURES ON HYDROLOGICAL PROCESSES

The new model structure includes epikarst zone overlain by soil and rock mixture, which is different from the original model structure of a solely soil zone. For the original model, the flow routing in the unsaturated soil zone is based on Equation (5); this equation is replaced by fracture flow Equation (8) for the new model. Additionally, the new model describes the uppermost soil zone with partially rock exposure (Equation (9)). For comparison of effects of the new model with the original model, three cases reflecting differences of flow medium between soil and fracture are set (Table II and Figure 13). The simulated results of hydrological processes in different medium properties reveal how epikarst zone and rock exposure influence hydrological processes.

For the study catchment with epikarst zone overlain by soil and rock mixture (case 1 in Table II), the new model can better simulate runoff processes of actual ET, total runoff and peak discharge (Table II) and capture fast rise and decline of flood discharges (Figure 13). Soil replacing fractured rock medium significantly increases ET loss and decreases flood discharge. If the uppermost layer of soil and rock mixture is replaced by the soil (for case 2 in Table II, ratio of rock exposure f_r in Equation (9) is equal to 0), actual ET increases to about

Table II. Observed and simulated actual evapotranspiration (ET), runoff, and peak discharge during the calibration and validation periods

	Calibration period (28 July 2007–19 October 2007)			Validation period (20 April 2008–30 December 2008)		
	ET (mm)	Runoff (mm)	Peak discharge (m^3/s)	ET (mm)	Runoff (mm)	Peak discharge (m^3/s)
Observation	—	171.2	0·956	—	773·9	1·527
Simulation (case 1)[a]	106·3	168·2	1·024	253·6	650·9	1·515
Simulation (case 2)[b]	142·1	164·4	0·798	298·6	627·7	1·104
	(33·6%)	(2·3%)	(−22·1%)	(17·7%)	(−3·6%)	(26·4%)
Simulation (case 3)[c]	149·8	168·8	0·236	320·9	581·1	0·473
	(40·9%)	(0·3%)	(−76·9%)	(26·5%)	(−10·7%)	(−68·7%)

[a] Epikarst zone overlain by soil and rock mixture.
[b] Epikarst zone overlain by soil solely.
[c] Epikarst zone replaced by soil.
Value in the blanket represents percentage of difference of simulated results for case 2 or case 3 in comparison with case 1. Peak discharge is the mean of peak discharges for all flood events.

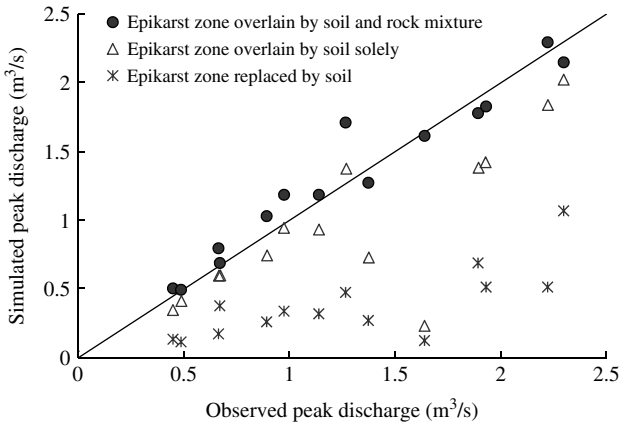

Figure 13. Scatter plot of observed *versus* simulated peak discharges for three cases of epikarst zone overlain by soil and rock mixture, epikarst zone overlain solely by soil, and epikarst zone replaced by soil

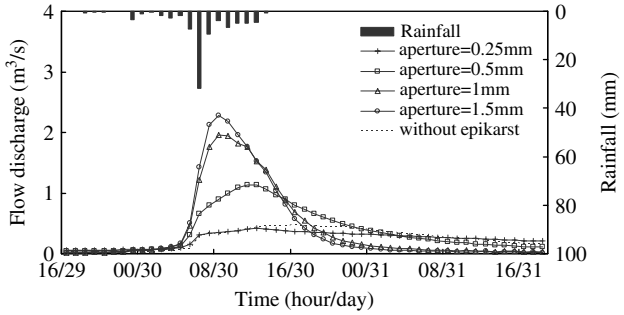

Figure 14. Comparison of simulated streamflow for different epikarst apertures

33·6 and 17·7%, and peak discharge values decrease to 20·0 and 26·4% during calibration and validation periods, respectively. If the uppermost zone is fully covered by the upper soil ($f_r = 0$) and epikarst zone is replaced by the lower soil (case 3 in Table II), simulated results using the original model demonstrate that actual ET increases about 40·8 and 26·5%, and peak discharge values decrease 76·9 and 68·8% during calibration and validation periods, respectively. Influence of rock exposure and epikarst zone on the total runoff is less significant during the calibration period of a rainfall season but more significant during the validation period including a drought season.

The new model can be used to simulate influences of rock fracture features on flow discharges because the hydraulic conductivity and discharge are a function of, and directly proportional to, the size of the aperture (i.e. an increase the aperture results in an increase in the hydraulic conductivity and an increase in the discharge). For scenarios of the fracture apertures with mean values of 0·25, 0·5, 1, and 1·5 mm and standard deviations of half mean values, simulated flow discharges, shown as Figure 14, demonstrate that 0·42 m^3/s of peak flow discharge for the aperture width of 0·25 mm increases to 2·29 m^3/s for a width of 1·5 mm. The peak discharge for the aperture larger than 1·0 mm occurs 2 h earlier than those of the smaller apertures. Figure 14 shows that flow recession becomes slower as the widths decrease.

Model simulation results show that fractural aperture controls the flood volume through influencing infiltrated rainfall division between unsaturated and saturated zones. A high density of fractures results in large infiltration and sharp hydrograph response, and thus, little infiltrated water remains in soil and gets eventually lost through ET. An example, shown in Figure 14, is the simulated streamflow for a scenario where the epikarst zone is replaced with the lower soil layer, compared with observed and simulated streamflow with epikarst during 29–31 July 2007. Basin average SMC of the upper and lower layers of the root zone overlying epikarst is 0·135 and 0·368, respectively, less than 0·158 and 0·390 when epikarst zone is replaced with soil. Consequently, basin actual ET increases from 0·047 to 0·070 mm/h.

CONCLUSIONS

As soil is very thin in the karst region of southwest China, hydrology in the karst basin is closely related to basin characteristics of fissured media in addition to topography, soil, and vegetation. This study showed that improving flow processes in the fractured zone of epikarst on the basis of the distributed hydrology-soil-vegetation model (DHSVM) could be used to simulate hydrological processes in the karst catchment. The improved model generally reproduced temporal variations in flow discharge at an underground outlet of Chenqi catchment with the coefficient of determination of larger than 0·75. Particularly, the improved model successfully captures the sharp variation in the hydrograph.

Parameterisation of the improved model was based on measured soil and fracture properties as well as model calibration. Detailed observation data of surface runoff, soil moisture content, and vegetation interception rate in addition to the observed flow discharge is an efficient way for the model calibration and reducing equivalence of different parameter combinations.

As the model structure has the distributed function in describing hydrology-soil and rock-vegetation, the model can be used to simulate soil moisture content and ET associated with precipitation, karst fractures, and vegetation cover. Simulated results show that just after a heavy rainfall event, distribution of soil moisture contents is closely related with topographic variations and SMCs at the upper soil layer are larger in the lower area than in the hillslopes because of water concentration into low areas. However, after a period of consecutive non-rainfall days SMCs are dominated by land covers due to ET. The upper layer soil in the forest cover areas has larger SMC than the shrub and agricultural areas, while the lower layer soil in the forest cover areas has less SMC than the shrubs and agricultural areas because ET is larger from the deep layer for forest, compared with those from the shallow layer in the shrub and bare soil areas. Spatial variation of the upper SMC is closely related with land covers, but the lower layer SMC is sporadic, indicating that the randomly distributed epikarst

fractures have significant influences on holding of its upper layer SMC.

Simulated results of hydrological processes in different medium properties reveal epikarst zone and rock exposure influences on hydrological processes. Increase of rock exposure rate and epikarst zone significantly decreases ET loss and increases flood discharge. If the whole water storage zone is replaced by soil, actual ET could increase about 40·8 and 26·5%, and peak discharge values decrease 76·9 and 68·8% during calibration and validation periods, respectively.

The discharge is directly proportional to the size of the aperture. As the fracture apertures increase from 0·25 to 1·5 mm, flow discharge could increase 5 times and the peak discharge occurs 2 h earlier.

Results of this study are helpful for the analyses of ecohydrological processes and are likely to help understand the response of these unique systems to major changes in land cover and land use.

ACKNOWLEDGMENTS

This research was supported by National Basic Research Program of China (973 Program) (No. 2006CB403200), National Natural Scientific Foundation of China (No. 40930635,51079038), the Key Project of China Ministry of Education (No. 308012), Programme of Introducing Talents of Discipline to Universities (No. B08048) and Program for Changjiang Scholars and Innovative Research Team in University, China. Thanks to the editor and two anonymous reviewers for their constructive comments on the earlier manuscript, which led to a great improvement of the paper.

REFERENCES

Aquilina L, Ladouche B, Doerfliger N. 2006. Water storage and transfer in the epikarst of karstic systems during high flow periods. *Journal of Hydrology* **327**: 472–485.

Bakalowicz M. 1995. La zone d'infiltration des aquifeŕes karstiques. Me'thodes d'e'tude. Structure et fonctionnement. *Hydrogeólogie* **4**: 3–2.

Beven KJ, Kirkby MJ. 1979. A physically based variable contributing area model of basin hydrology. *Hydrological Sciences Bulletin* **24**(1): 43–69.

Beven KJ. 1989. Changing ideas in hydrology-The case of physically based models. *Journal of Hydrology* **105**: 157–172.

Brooks RH, Corey AT. 1964. *Hydraulic properties of porous media: Hydrology Papers*. Colorado State University; pp.24.

Chen X, Chen C, Hao Q, Zhang Z, Shi P. 2008. Simulation of rainfall-underground outflow responses of a karstic watershed in southwestern China with an artificial neural network. *Water Science and Engineering* **1**(2): 1–9.

Chen X, Zhang ZC, Chen XH, Shi P. 2009. The impact of land use and land cover changes on soil moisture and hydraulic conductivity along the karst hillslopes of southwest China. *Environmental Earth Sciences* **59**: 811–820.

Diersch H-JG, Michels I. 1995. 3D-Finite-Element-Modellierung von Strömungs-, Schadstoff- und Wärmetransportprozessen im Grundwasser mit freien und ohne freie Oberflächen. *Einsatz von DV-Methoden im Umweltbereich Schriftenreihe des BDG.* **14**(14): 53–55.

Einsield F. 2005. Flow system dynamics and water storage of a fissured-porous karst aquifer characterized by artificial and environmental tracers. *Journal of Hydrology* **279**(1): 312–321.

Field MS. 1997. Risk assessment methodology for karst aquifers:(2) solute-transport modeling. *Environmental Monitoring and Assessment* **47**: 23–37.

Field MS, Nash SG. 1997. Risk assessment methodology for karst aquifers: (1) estimating karst conduit-flow parameters. *Environmental Monitoring and Assessment* **47**: 1–21.

Fleury P, Plagnes V, and Bakalowicz M, 2007. Modelling of the functioning of karst aquifers with a reservoir model: Application to Fontaine de Vaucluse (South of France). *Journal of Hydrology.* **345**: 38–49.

Ford DC, Williams PW. 1989. *Karst Geomorphology and Hydrology*. Unwin Hyman: London.

Ford DC, Williams PW. 2007. *Karst Hydrogeology and Geomorphology*. Wiley: Chichester; pp. 561.

Gouisset Y. 1981. Le karst superficiel: gene'se, hydrodynamique et caracte'ristiques hydrauliques. University des Sciences et techniques du Languedoc: Montpellier, France; 218.

Hao Y, Yeh T-CJ, Gao Z, Wang Y, Zhao Y. 2006. A gray system model for studying the responses to climatic change: the Liulin karst springs, China, *Journal of Hydrology.* **328**: 668–676.

Harbaugh AW. 2005. MODFLOW-2005, the US Geological Survey modular ground-water model- the Ground-Water Flow Process. USGS: US; 20–36.

Király L. 1969. Anisotropie et hétérogénéité de las perméabilité dans les calcaires fissurés. *Eclogae Geologica Helvetiae* **62**(28): 613–619.

Kovács A. 2003. *Geometry and hydraulic parameters of karst aquifers: A hydrodynamic modeling approach.* thése, Université de Neuchâtel, Suisse.

Leij FJ, Alves WJ, Thvan Genuchten M, Williams JR. 1996. *The UNSODA unsaturated soil hydraulic database. version 1·0*, EPA report EPA/600/R-96/095, EPA National Risk Management Laboratory, G-72, Cincinnati, OH. Available at: http://www.ussl.ars.usda.gov/MODELS/unsoda.htm.

Lu Y. 2007. Karst water resources and geo-ecology in typical regions of China, *Environmental Geology* **51**: 695–699.

Milanovic PT. 1981. *Karst Hydrogeology*. Water Resources Publications: Littleton, Colorado; pp. 434.

Peng T, Wang SJ, Zhang XB, Rong L, Chen B, Yang T, Wan JY. 2008. Results of preliminary monitoring of surface runoff coefficients for karst slopes. *Earth and Environment* **36**(2): 125–129 (in Chinese).

Perrin J, Jeannin PY, Zwahlen F. 2003. Epikarst storage in a karst aquifer: a conceptual model based on isotopic data, Milandre test site, Switzerland. *Journal of Hydrology* **279**: 106–124.

Scanlon BR, Mace RE, Barrett ME, Smith B. 2003. Can we simulate regional groundwater flow in a karst system using equivalent porous media models? Case study, Barton Springs Edwards aquifer, USA. *Journal of Hydrology* **276**: 137–158.

Singhal BBS, Gupta RP. 1999. *Applied hydrogeology of fractured rocks.* Kluwer Academic Publisher: Dordrecht, the Netherlands.

Smart PL, Friederich H. 1986. Water movement and storage in the unsaturated zone of a maturely karstified carbonate aquifer, Mendip Hills, England. In: *D. National Water Well Association, Ohio (Ed.), Proceedings of the Conference on Environmental Problems of Karst Terrains and their Solutions*. pp. 59–87.

Snow DT. 1969. Anisotropic permeability of fractured media, *Water Resources Research* **5**(6): 1273–1289.

Sun AY, Painter SL, Green RT. 2005. Modeling Barton Springs segment of the Edwards aquifer using MODFLOW-DCM. *Proceedings of Sinkholes and the Engineering and Environmental Impacts of Karst*: 163–168.

Tan XQ, Jiang ZC. 2005. A Review of recent advances and perspective in epikarst water study. *Carsologia Sinica* **24**(3): 250–254 (in Chinese).

Teutsch G. 1993. An extended double-porosity concept as a practical modeling approach for a karstified terraine. In *Hydrogeological Processes in Karst Terraines, Proceedings of the Antalya Symposium and Field Seminar*, Gultekin, Johnson, and Back (eds). *October 1990: International Association of Hydrological Sciences*, vol. 207, 281–292.

Wang S, Rong L, Du X, Ge Y. 2008. Water source partitioning and water use strategy among karst trees growing on shallow karst: perspectives from stable isotope composition. *Bulletin of Mineralogy, Petrology and Geochemistry* **27**(z1): 513–514.

White WB. 1988. *Geomorphology and Hydrology of Karst Terrains*. Oxford University Press: New York.

White WB. 1999. Groundwater flow and transport in karst. In *The Handbook of Groundwater Engineering* Delleur JW (ed), CRC Press LLC: USA.

White WB, Deike GH. 1989. Hydraulic geometry of cave passages. In *Karst Hydrology: Concepts from the Mammoth Cave Area*, White WB, White EL (eds), Van Nostrand Reinhold: New York; Ch. 9.

Wigmosta MS, Vail LW, Lettenmaier DP. 1994. A distributed hydrology-vegetation model for complex terrain. *Water Resources Research* **30**(6): 1665–1679.

Williams PW. 1985. Subcutaneous hydrology and the development of doline and cockpit Karst. *Zeitschriftfu̇r Geomorphologie NF* **29**: 463–482.

Williams PW. 2008. The role of the epikarst in karst and cave hydrogeology: a review. *International Journal of Speleology* **37**(1): 1–10.

Xiang C, Song L, Zhang P, Pan G, Wang J. 2004. Preliminary study on soil fauna diversity in different vegetation cover in Shilin National Park, Yunnan, China. *Resources Science* **26**: 98–103.

Xue X, Chen X, Zhang Z, Wei L. 2009. Effect of karst fracture on saturated subsurface flow confluence. *Water Resources and Power* **27**(6): 20–23 (in Chinese).

Yuan DX, Cai GH. 1988. *The science of karst environment*. Chongqing Press: Chongqing, China (in Chinese).

